

# Imaging of Photonic Crystal Localized Modes through Third-Harmonic Generation

Yijia Zeng,<sup>†</sup> Iannis Roland,<sup>†</sup> Xavier Checoury,<sup>†</sup> Zheng Han,<sup>†</sup> Moustafa El Kurdi,<sup>†</sup> Sébastien Sauvage,<sup>†</sup> Bruno Gayral,<sup>‡,||</sup> Christelle Brimont,<sup>§</sup> Thierry Guillet,<sup>§</sup> Fabrice Semond,<sup>⊥</sup> and Philippe Boucaud<sup>\*,†</sup>

<sup>†</sup>Institut d'Electronique Fondamentale, CNRS, Université Paris-Sud, Université Paris-Saclay, Bâtiment 220, Rue André Ampère, F-91405 Orsay, France

<sup>‡</sup>Université Grenoble Alpes, F-38000 Grenoble, France

<sup>§</sup>Laboratoire Charles Coulomb (L2C), UMR 5221, CNRS-Université de Montpellier, F-34905 Montpellier, France

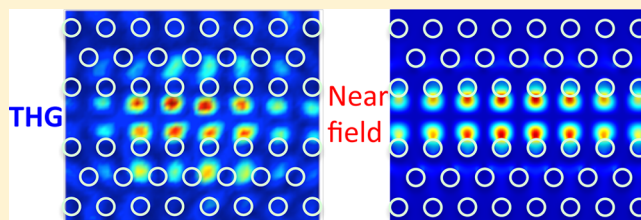
<sup>⊥</sup>CRHEA-CNRS, Rue Bernard Grégory, F-06560 Valbonne, France

<sup>||</sup>CEA, INAC-PHELIQS, CEA-CNRS Group "Nanophysique et Semiconducteurs", F-38000 Grenoble, France

## Supporting Information

**ABSTRACT:** We demonstrate high-spatial resolution imaging of localized cavity modes through third-harmonic frequency conversion. The experiments are performed with a III-nitride-on-silicon photonic platform. The resonant cavities are formed within suspended two-dimensional photonic crystals and are excited with a continuous-wave excitation around 1550 nm. The III-nitride materials (GaN and AlN) are transparent for both pump and harmonics. The third-harmonic nonlinear process allows one to indirectly observe the fundamental confined cavity mode with spatial profiles equivalent to those usually obtained by local probe microscopy techniques such as scanning near-field optical microscopy. An excellent agreement is obtained between the measured polarization-resolved third-harmonic emission patterns and those calculated through the third-order nonlinear polarization. We show that the spatial profiles of the radiated patterns are strongly dependent on defocusing, thus highlighting the strong sensitivity of the imaging.

**KEYWORDS:** photonic crystal, third-harmonic generation, subwavelength imaging, III-nitride semiconductors



Second- and third-harmonic generation are well-known techniques to produce high spatial resolution imaging.<sup>1,2</sup> These techniques are commonly used in biology to image living cells along with multiphoton imaging such as two-photon excitation fluorescence.<sup>3–5</sup> The frequency conversion gives access to smaller wavelengths and consequently to better spatial resolution since the constraint on the diffraction limit is relaxed. A specific feature of the nonlinear process is the reduction of the interaction volume that can lead to the observation of sharper features with an enhanced resolution.<sup>6</sup> Moreover, the nonlinear susceptibility tensors are also dependent on the local symmetry and orientations and can more easily reveal interfaces or local changes of the susceptibility. In photonic crystals, harmonic generation has mainly been used for frequency conversion and the transfer of a coherent emission to shorter wavelengths. The frequency conversion takes advantage of high quality factors and small modal volumes that enhance the nonlinear interactions.<sup>7–9</sup> Moreover it allows one to perform nonlinear experiments with cavities or slow-light modes using low-power continuous wave excitations as opposed to the pulsed ultrafast and high-intensity laser systems commonly used in nonlinear optics.

Imaging of photonic crystal localized modes around 1550 nm with a microscope is limited by diffraction and does not reveal

fine details. It explains why most of the studies performed on photonic crystals either with embedded emitters as internal sources<sup>10–12</sup> or external excitation were performed in the spectral domain, without probing the spatial profile of the confined optical modes. Alternately, Fourier-space imaging of localized modes was performed by several groups.<sup>13,14</sup> In principle, a better resolution would be expected if one uses harmonic generation. Moreover, harmonic generation can provide distinct information as compared to fluorescence microscopy as a consequence of the coherent process and its sensitivity to phase information, as shown for example in the study of biological samples.<sup>15</sup> To date, images of emission patterns associated with second-harmonic generation have been obtained in two-dimensional photonic crystals, but they did not reveal very sharp structures.<sup>16–21</sup>

In this article, we show that third-harmonic generation is a powerful technique to image localized modes resonant around 1550 nm with a high subwavelength spatial resolution. The experiments are performed with a gallium nitride on silicon photonic platform. Harmonic conversion has already been successfully demonstrated in photonic crystals fabricated from

Received: April 5, 2016

Published: May 31, 2016

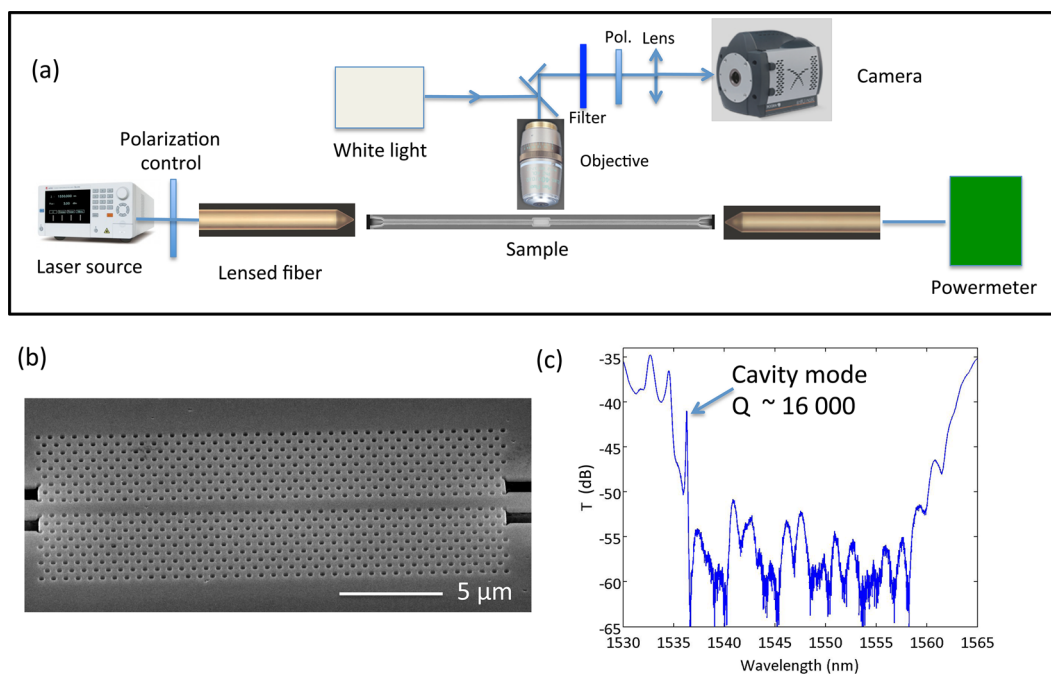


**Figure 1.** (a) Schematics of the experimental setup used to measure the third-harmonic emission. Light is injected in the layer plane with an in-plane  $E$ -field perpendicular to the long direction of the sample. The third harmonic is collected from the surface. (b) Scanning electron microscopy image of the free-standing gallium nitride photonic crystal on silicon. (c) Transmission spectrum of a cavity where only the second and third row of holes around the cavity center have been displaced. The maximum displacement is 4 nm. The cavity resonance is observed at 1536.5 nm. The quality factor is 16 000.

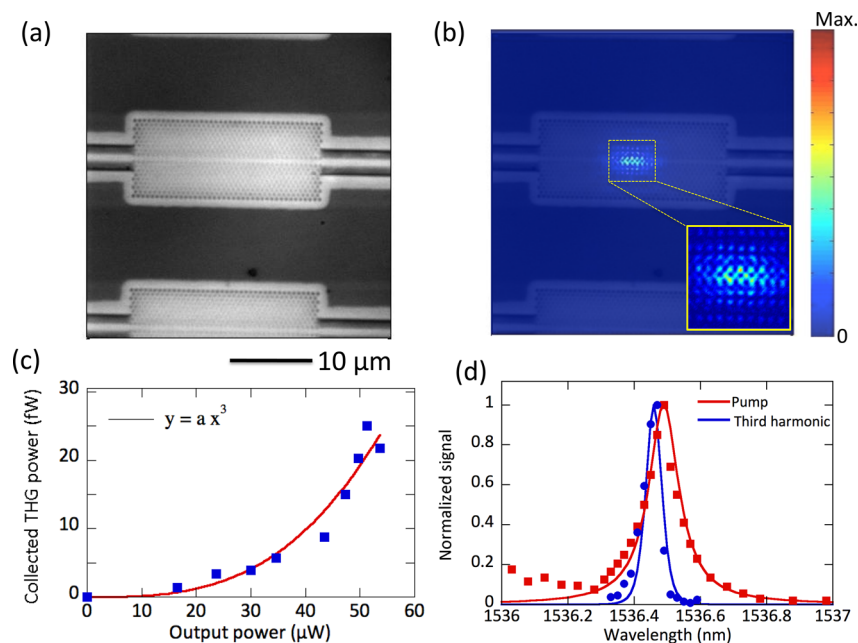


**Figure 2.** (a) Optical microscopy image of the sample surface measured with white light illumination. The total size of the image is 36.8  $\mu\text{m}$ . (b) Third-harmonic emission pattern measured when the cavity is pumped in resonance superimposed with the optical image of the structure. The inset shows a zoom-in of the third-harmonic signal. The signal is not polarization-resolved. (c) Dependence of third-harmonic collected power as a function of the output power at the exit of the photonic crystal. The latter is proportional to the energy inside the cavity. The maximum power at the entrance of the photonic crystal is 14 mW in this experiment. The full line is a cubic power law fit. (d) Spectral dependence of the third-harmonic signal compared to the cavity resonance. The squares and dots correspond to experimental data. A narrowing is observed as a consequence of the third-order nonlinear process. The red full line is a Lorentzian fit, while the full blue line is the cubic power of the Lorentzian used to fit the fundamental mode. The curve has been only slightly spectrally shifted to match the experimental data.

the III-nitride materials<sup>21–24</sup> or in microring resonators.<sup>25</sup> Here we observe for the first time resonant frequency tripling in a III-nitride photonic crystal cavity under continuous wave excitation

around 1550 nm. We show that with a microscope objective of numerical aperture lower than 1, high spatial resolution images of the confined modes can be obtained. The third-harmonic

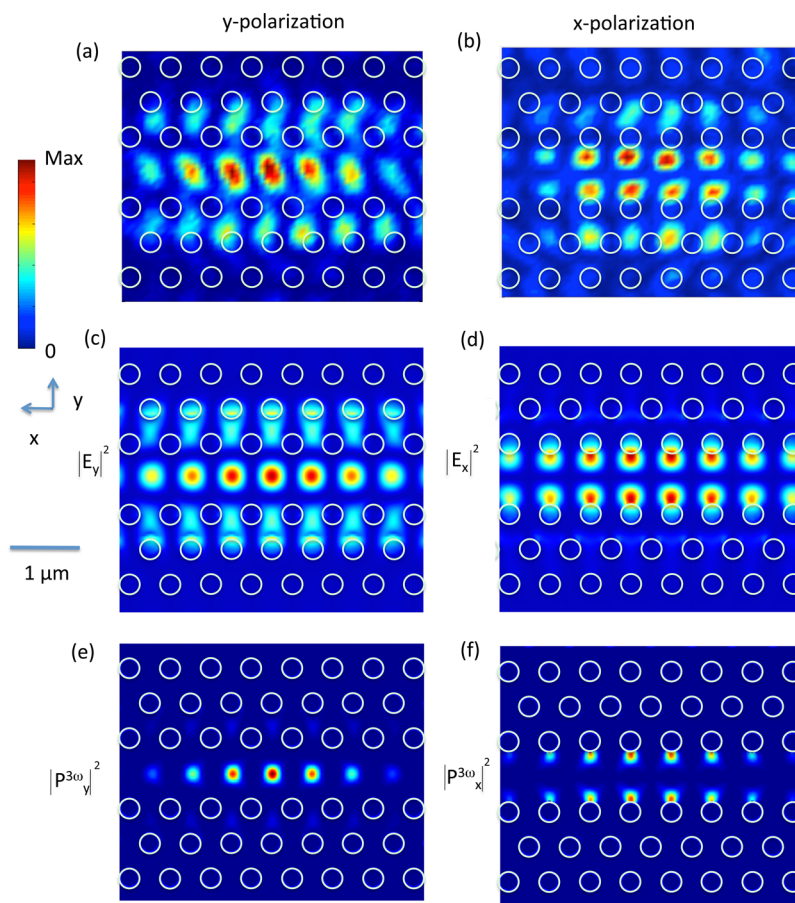


**Figure 3.** (a) Zoom-in of the experimental third-harmonic emission pattern for a polarization  $E_y$  perpendicular to the waveguide axis. The photonic crystal holes have been schematically superimposed on the image. (b) Zoom-in of the third-harmonic emission for the polarization along the waveguide axis  $E_x$ . (c) Near-field profile of the square modulus of the electric fields ( $|E_y|^2$ ) of the cavity mode for the  $E_y$  polarization and  $E_x$  polarization (d) calculated by 3D-FDTD. The cavity is a width-modulated waveguide cavity with a maximum hole displacement of 6 nm ( $Q = 18\,000$ ). (e) Square modulus of the third-harmonic polarization  $|P_y^{3\omega}|^2$  calculated by 3D-FDTD. (f) Square modulus of the third-harmonic polarization  $|P_x^{3\omega}|^2$  calculated by 3D-FDTD.

generation images reveal resonant spots with a diameter less than 300 nm and very high contrast. These features directly originate from the interaction between the localized electric field of the cavity fundamental mode and the nonlinear susceptibility tensor to create a third-order polarization polarized in the layer plane. Polarization-resolved images show that the images can be directly associated with the  $E_x$  and  $E_y$  in-plane electric field components through the  $\chi_{xxxx}^{(3)}$  and  $\chi_{yyyy}^{(3)}$  elements. In these structures, the third-harmonic emission patterns provide a spatial mapping equivalent to the one obtained by more complex approaches such as scanning near-field optical microscopy when probing cavity fundamental modes around 1550 nm.<sup>26–28</sup> These experiments emphasize the interest in nonlinear imaging as a very simple *in situ* technique to reveal localized patterns in photonic crystals, without any sample preparation. This can be achieved if no confined modes are resonant at the third-harmonic wavelength.

## DESCRIPTION OF SAMPLES AND MEASUREMENT SETUP

We have developed the fabrication of two-dimensional photonic platforms with III-nitride directly grown on silicon(111) by molecular beam epitaxy, which enables the use of a low-cost large-area silicon substrate.<sup>29–31</sup> The interest of this chip-scale integrated platform is manifold: nitride

materials such as AlN or GaN are transparent for wavelengths above  $\lambda/3$ , thus allowing the propagation of pump and harmonics for an excitation wavelength around 1550 nm. The fabricated structures consist of a thin AlN layer, around 45 nm thickness, epitaxially grown on silicon followed by a 300 nm thick GaN layer. The two-dimensional photonic circuits were fabricated by a succession of electron-beam lithography, chlorine-based plasma etching, and selective under-etching between nitride and silicon with  $\text{XeF}_2$ .<sup>32</sup> The selective etching between the III–V semiconductors and silicon enables the easy fabrication of self-standing structures. They consist of suspended waveguides and free-standing two-dimensional photonic crystal membranes. The total length of the sample is 500  $\mu\text{m}$ , and the photonic crystal with a 23.4  $\mu\text{m}$  length stands at the middle of the structure. The photonic crystal consists of a W0.98 waveguide corresponding to a width of  $0.98\sqrt{3}a$ , where  $a$  is the 580 nm photonic crystal lattice period. The hole radius to period ratio was around 0.23. At the middle of the photonic crystal, we have designed width-modulated waveguide cavities either by only displacing the second and third row of holes perpendicularly to the waveguide axis or following the A1 design presented in ref 33 (samples used in Figures 3 and 5 for the latter case). Modeling indicates that the cavities where only the second and third row of holes are

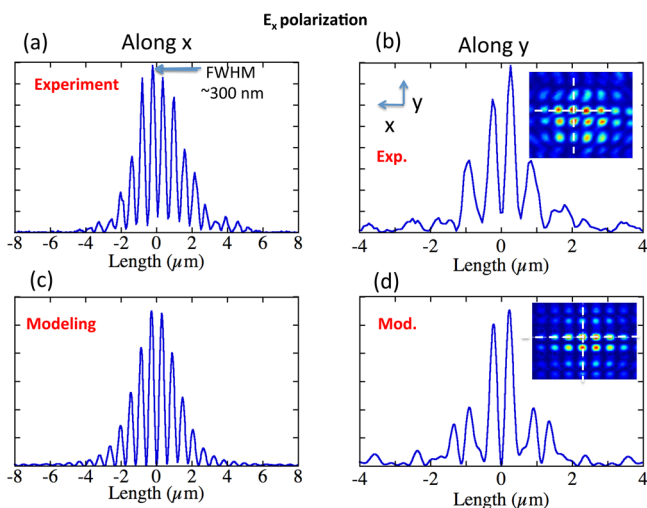


**Figure 4.** (a) Experimental cross-section along the  $x$  direction of the third-harmonic radiated pattern for  $E_x$  polarization. (b) Experimental cross-section along the  $y$  direction. The positions of the cross sections are marked on the inset. (c) Calculated cross-section along the  $x$  direction. (d) Calculated cross-section along the  $y$  direction. The inset shows the position of the cross-section lines.

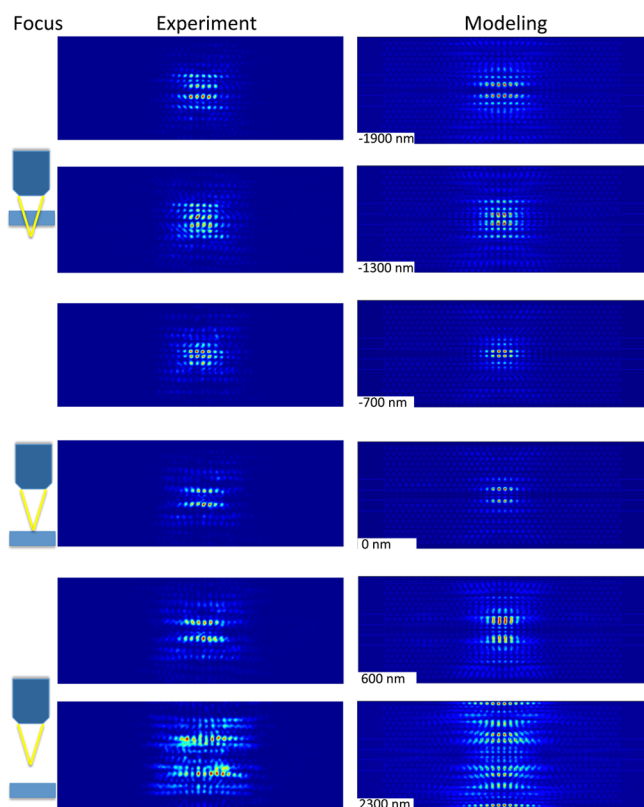


**Figure 5.** Comparison between measured (left panel) and calculated (right panel) third-harmonic radiated patterns for different focus distances. As shown schematically on the left of the image, the focus plane varies from below the sample (top) to above the sample (bottom). In the modeling, this corresponds to focus distances varying from  $-1900$  to  $+2300$  nm, measured from the top surface of the sample. The measurements and modeling correspond to the  $E_x$  polarization. For each image, the maximum amplitude of the signal is normalized to 1. Experimentally under white light illumination, the focus for the photonic crystal image as shown in Figure 2a is obtained for the  $-700$  nm distance.

displaced can also support high quality factors for hole displacements larger than in the design of ref 33.

For the experiments, we use a tunable continuous-wave laser source coupled to an erbium-doped amplifier. Light is injected with lensed fibers, and the coupling of light in the structure is enhanced with inverted tapers.<sup>34</sup> Light injection is optimized by monitoring the transmission in a spectral range spanning from 1500 to 1600 nm. The maximum output power delivered by the fiber amplifier is 18.6 dBm, which corresponds to 14 mW at the entrance of the photonic crystal. It is remarkable that the resonant enhancement with a cavity mode allows one to obtain images of harmonic emission with a low-power continuous-wave excitation as opposed to pulsed and ultrafast lasers commonly used in harmonic imaging experiments. All experiments are performed at room temperature. The harmonic signal is collected perpendicular to the surface using an objective with a numerical aperture of 0.9. The scattered light from the optical pump is rejected through band-pass filters. An interference filter centered around the frequency-tripled pump signal was inserted in order to image only the third-harmonic signal. The emission patterns were recorded with a photon-counting electron multiplying charge coupled device camera. The camera has  $512 \times 512$  pixels with  $16 \mu\text{m}$  pixel size, and as the effective optical magnification is 220, one pixel represents 72 nm on the surface. White light illumination through the microscope objective is also available for alignment and imaging of the cavities. A schematic of the whole measurement setup is shown in Figure 1a. Figure 1b shows a scanning electron microscopy image of the free-standing nitride photonic crystal on silicon.

The transmission spectrum of one investigated cavity is shown in Figure 1c. The cavity exhibits a resonant cavity mode with a quality factor of 16 000 at 1536.5 nm. We note that for harmonic generation experiments, there is a trade-off between the quality factor and the transmission since the harmonic conversion depends on the energy that is stored in the cavity. This energy is to first order proportional to the quality factor times the square root of the global transmission of the photonic crystal. The photonic crystal cavity has only a single marked resonance for the fundamental mode. No photonic band gap exists at the third-harmonic wavelength in the visible range around 510 nm.

### THIRD-HARMONIC CHARACTERIZATION

Figure 2a shows an image of the sample surface recorded under white light illumination with the same setup as for the measurement of the harmonic pattern. Figure 2b shows a superposition of this structural image with the third-harmonic emission excited by the continuous-wave laser resonant with the cavity mode. The inset shows a zoom-in of this image, which will be discussed later. The harmonic emission is strongly localized, typically  $8 \mu\text{m}$  along the waveguide direction. It is observed at the photonic crystal center where the cavity stands. No signal is observed either in the access waveguide nor at the entrance of the photonic crystal. This image illustrates the strong enhancement of the emission due to the resonant cavity mode. The harmonic conversion can be observed with continuous-wave excitation even if the third-order nonlinear susceptibility is small in the near-infrared range since the third-harmonic resonance is still below the band gap, a situation completely different from the one encountered in silicon.<sup>35</sup>

Figure 2c shows the dependence of the integrated third-harmonic signal as a function of the power measured at the

output of the structure that is proportional to the energy present in the cavity.<sup>36</sup> If we neglect the harmonic conversion and the residual losses, one expects in a triply resonant system at low power  $P^{(3\omega)} = \frac{256}{3\omega^2} \eta^3 \eta_3 Q^3 Q_3 |\beta|^2 P^3$  for this third-order nonlinear process, where  $\eta$  ( $\eta_3$ ) is the coupling efficiency for the pump (third harmonic),  $Q$  ( $Q_3$ ) the quality factors of the pump (third harmonic),  $\beta$  an overlap integral between the pump field and the third-harmonic field, and  $P$  the incident power.<sup>7,19</sup> Note that the  $\beta$  overlap factor between pump and harmonic corresponds to the phase-matching requirement considered for the conversion of propagating modes. For a simply resonant system, the harmonic power is proportional to the cube of the power present in the cavity. In the present experiments, we have not attempted to achieve phase matching and to obtain a resonant cavity mode for the third harmonic.<sup>37</sup> The photonic crystal exhibits a continuum of modes at the third-harmonic frequency. As seen in Figure 2c, the signal indeed exhibits a cubic dependence, as evidenced by the full line that is best fit by a cubic power law, the contribution of lower order terms being negligible. We note that these types of cavities also support second-harmonic generation with a  $z$ -oriented polarization, but with a weak efficiency. The present signal is well accounted for by a third-harmonic process without considering linear mixing of a second harmonic and pump.

In Figure 2d, we compare the spectral dependence of the third-harmonic signal with the spectral dependence of the pump mode. The input laser power is kept constant (15.5 dBm at the laser output). A spectral narrowing is observed with a line width reduction from 110 pm for the pump to 57 pm for the harmonic (equivalent  $Q$  factor of 9000). This is a direct consequence of the third-order process and the cubic dependence described above. The harmonic signal can be fitted by a cubic Lorentzian,<sup>18</sup> as shown by the full line in Figure 2d.

## ■ HIGH-RESOLUTION IMAGING

Figure 3 shows an enlargement of the third-harmonic emission patterns for two distinct polarizations. The experiments have been performed with an A1 cavity design following ref 33 with a maximum hole displacement of 6 nm. The quality factor of this cavity is 18000. Figure 3a corresponds to an electric field perpendicular to the waveguide/cavity axis ( $E_y$ ), while Figure 3b corresponds to a polarization along the waveguide axis ( $E_x$ ). We have superimposed on the images the photonic crystal pattern. Several features can be observed. The third-harmonic pattern is composed by well-defined spots with a typical full width at half-maximum smaller than 300 nm, as shown in Figure 4. This has to be compared with the 1530 nm excitation wavelength and will be discussed in the next section. A high-intensity contrast is obtained up to 90%. The signal dynamics is sufficiently important to observe regularly spaced lines with an almost vanishing signal along the  $x$ - or  $y$ -axis (see Figure 4). The symmetry properties and profile of the third-harmonic pattern are related to those of the fundamental cavity mode. The profiles of the square modulus of the electric fields  $|E_y|^2$  and  $|E_x|^2$  calculated by the three-dimensional finite-difference, time-domain (FDTD) method are shown for comparison in Figure 3 c and d. The detailed modeling of the third-harmonic emission pattern will be discussed in the next section. The objective of the comparison between Figure 3a,b and c,d is not to make a direct connection between the images but to illustrate the link between the third-harmonic profile and the

near-field spatial distribution of the fundamental mode around 1.5  $\mu\text{m}$ . We do observe the same symmetry and more importantly similar in-plane extension of the spots. Figure 3e and f show the calculated squared magnitude of the third-order polarization. This third-order polarization generates the observed  $\eta$  signal in the visible. The same symmetry properties are observed for the third-order polarization and for the third-harmonic images. The spatial extension of the bright spots is smaller as compared to the magnitude of the electric field at 1530 nm as a result of the third-order nonlinear process. We note that the correspondence between the third-order polarization and the experimental pattern can be obtained as long as no resonant modes with a significant  $Q$  factor are present for the third-harmonic signal. This is the case in the present experiments; otherwise the radiated pattern could be modified.

## ■ SIMULATION OF THIRD-HARMONIC EMISSION PATTERNS

In order to interpret the image of the collected third harmonic, we have calculated the third-harmonic polarization that is generated by the fundamental mode of the cavity. The fundamental mode profile was obtained by three-dimensional finite-difference time domain modeling as shown in Figure 3c and d. For the harmonic polarization calculation ( $P_i^{(3\omega)} = \sum \epsilon_0 \chi_{ijkl}^{(3)} E_j E_k E_l$  where  $E$  is the cavity mode electric field), one has to consider the different orientations of the third-order nonlinear susceptibility for the III-nitride material. The  $x$ -axis is along the waveguide axis, the  $y$ -axis is perpendicular to the waveguide, and the  $z$ -axis is along the growth direction. The main components of the electric field are the  $E_x$  and  $E_y$  components, and we have neglected the  $E_z$  component, which has a much smaller amplitude. The components of interest of the susceptibility tensor are thus  $\chi_{xxxx}^{(3)}$ ,  $\chi_{yyyy}^{(3)}$ , and  $\chi_{yyxx}^{(3)}$  and their permutations.<sup>38</sup> In the modeling presented below, we have also considered the  $\chi_{yyxx}^{(3)}$ -type components even if their amplitude is reduced by a third as compared to  $\chi_{xxxx}^{(3)}$ . As the amplitudes of  $\chi_{xxxx}^{(3)}$  and  $\chi_{yyyy}^{(3)}$  are larger than the cross-correlation terms for tetragonal lattices, there is a quasi-direct link between the  $x(y)$ -polarized third-order polarizations and the  $x(y)$  components of the fundamental mode. The third-order polarization is thus predominantly polarized in the layer plane. The third-order polarization has been calculated for different axis orientations in the layer plane. There is almost no change in the polarization when the axis is rotated by 30°, 45°, 60°, and 90°.

Once the polarization is calculated, its spatial profile is injected as a source term in the FDTD modeling. In the Fourier domain, we take into account the  $E$  and  $H$  field propagation through a phase-propagating term and filter the Fourier components by the objective numerical aperture. We then calculate the time-averaged Poynting vector.<sup>21</sup>

Figure 4 shows a comparison of the cross-sections for the  $E_x$  polarization between the calculated radiated pattern and the measured ones. Figure 4a and c correspond to the  $x$  direction, while Figure 4 b and d correspond to the  $y$  direction. The cross-sections show that the full-width at half-maximum of the bright spots is less than 300 nm. Several features need to be emphasized. The spatial distribution information is identical to the typical ones that can be obtained by scanning near-field optical microscopy through the field mapping of electromagnetic fields.<sup>27,28</sup> This feature is linked with the microscope resolution at the third-harmonic wavelength as given by the

Rayleigh criterion ( $0.61\frac{\lambda}{NA}$ ), where NA is the numerical aperture of the objective (0.9). The experimental resolution of the measurement can be estimated from the comparison between Figure 4a and c. The modeling in Figure 4c accounts for the 0.9 numerical aperture of the objective. An excellent agreement is obtained when comparing with the experimental radiated pattern. The  $\sim 300$  nm resolution is thus about  $\frac{\lambda}{5}$  when compared to the wavelength of the fundamental mode. The measurement of the resonant third harmonic thus provides an indirect imaging of the photonic crystal fundamental mode with a subwavelength resolution.

As compared to scanning near-field techniques, the harmonic experiments can be performed *in situ*, without any sample preparation and is not plagued by artifacts that can occur in local probe microscopies. Moreover, one does not perturb the confined mode with a tip being approached close to the cavity, like an aperture probe or an apertureless tip, to convert the near-field to far-field information. The technique can thus be applied to cavity modes with high Q factors even above a million as obtained, for example, in silicon photonic crystals.<sup>34</sup> Here, through third harmonics and without a specific and expensive local probe apparatus to retrieve the near-field information, the same spatial information can be obtained by using a simple microscope objective and by looking at the near-field third-harmonic radiated pattern filtered by the optical setup.

## EFFECT OF DEFOCUSING

In real-space imaging, the recorded images can be strongly dependent on defocusing. Figure 5 shows a comparison between the measured and calculated radiated patterns for the  $E_x$  polarization for various focus distances. The focus distance varies regularly from  $-1900$  to  $+2300$  nm measured from the sample top surface. The top image corresponds to a focus plane below the suspended membrane ( $-1900$  nm), while the bottom image corresponds to a focus above the sample ( $+2300$  nm). Supplementary S1 shows a movie of the calculated radiated patterns as a function of defocusing. The striking feature is the very strong dependence of the third-harmonic pattern as a function of defocusing. One obtains profiles that differ significantly depending on the position of the collection objective and that are not symmetrical with respect to the suspended membrane vertical center. This is a consequence of the change of the microscope optical transfer function as a function of focusing as well as the interference effects between the multiple coherent radiating dipoles.<sup>39</sup> The spatial profile shown in Figure 3b that is the most closely related to the near-field profile for the  $E_x$  polarization corresponds to a theoretically calculated defocus distance of  $-700$  nm. The versatility of the profiles is also a consequence of the transparency of the nitride material at the third-harmonic frequency. This could not be obtained for example with silicon or GaAs samples with the pump at this wavelength. The second striking feature is the excellent agreement that is reported between experimental radiated patterns and the calculated ones. One can observe in Figure 5 that all the salient features observed experimentally are accounted for in the modeling. The horizontal and vertical extensions are similar between experiment and modeling. One clearly observes that the vertical displacement of the spots with the largest amplitude are positioned on the first row of holes at  $-1900$  nm, at the center

of the waveguide at  $-700$  nm, at the first row of holes at  $0$  nm, and then between the first and second row of holes at  $600$  nm. We do not observe a strict periodicity of the patterns as in the Talbot self-imaging due to the interferences of diffracted beams when the focus distance is varied along the  $z$  direction.<sup>40,41</sup> In the latter case, the textbook model corresponds to a periodic grating illuminated on a large surface by a plane wave. In the paraxial approximation where the wavelength  $\lambda$  is considered small as compared to the grating period  $\Lambda$ , the Talbot length  $2\frac{\Lambda^2}{\lambda}$  would be  $1300$  nm. In the present experiments, the source dipoles are tightly localized by the cavity mode and the experimentally observed spatial patterns evolve as we scan along the positive  $z$  direction, without strictly repeating themselves over multiple periods.

These measurements highlight the high sensitivity of third-harmonic imaging since a small deviation from the collection distance can lead to significantly different radiated patterns. The modeling justifies that spatial profiles of third-harmonic radiated patterns similar to the near-field profile can indeed be obtained. It also indicates that third-harmonic defocusing microscopy is a very rich tool to study the properties of coherent scattering media. We expect to investigate these phenomena in more detail in future work by considering higher quality factor cavities. Such cavities can be obtained in nontransparent media such as silicon, where quality factors larger than one million can be reached.<sup>34</sup>

## CONCLUSION

In conclusion, we have observed resonant third-harmonic generation under continuous wave excitation in free-standing gallium nitride photonic crystal cavities fabricated on a silicon substrate. We have shown that the third-harmonic conversion is a powerful tool to observe the spatial features of the fundamental exciting modes. By converting the excitation wavelength to the visible range, we strongly minimize the limitation on spatial resolution due to diffraction. Spatial features with spot sizes as small as  $300$  nm were resolved for an excitation wavelength of  $1530$  nm. An excellent agreement was obtained between the spatially resolved measurements and the modeling of the radiated pattern. With these experiments, we are thus able to achieve a subwavelength resolution and a quality of imaging equivalent to that obtained by near-field techniques when probing  $1550$  nm cavity modes localized by photonic crystal design. The advantage of third-harmonic generation imaging is the simplicity of the approach, since only a microscope objective and a CCD camera are needed, and the ability to perform it without perturbing the confined mode. We expect that this technique will be implemented to study other types of photonic crystal devices, e.g., slow-light waveguides, fabricated from III-nitride materials or other semiconductors.

## ASSOCIATED CONTENT

### Supporting Information

The Supporting Information is available free of charge on the ACS Publications website at DOI: 10.1021/acsphtonic.6b00236.

Description of movie (PDF)

Movie highlighting the results of modeling as a function of defocusing as shown in Figure 5 (AVI)

## ■ AUTHOR INFORMATION

## Corresponding Author

\*E-mail: philippe.boucaud@ief.u-psud.fr.

## Notes

The authors declare no competing financial interest.

## ■ ACKNOWLEDGMENTS

This work was supported by Agence Nationale de la Recherche under the QUANONIC convention (ANR 2013BS10-0010-03). This work was also partly supported by the RENATECH network. We acknowledge support by a public grant overseen by the French National Research Agency (ANR) as part of the "Investissement d'Avenir": program: Labex GANEX (Grant No. ANR-11-LABX-0014) and Labex NanoSaclay (reference: ANR-10-LABX-0035). We thank Jean-Yves Duboz for fruitful discussions.

## ■ REFERENCES

- (1) Barad, Y.; Eisenberg, H.; Horowitz, M.; Silberberg, Y. Nonlinear scanning laser microscopy by third harmonic generation. *Appl. Phys. Lett.* **1997**, *70*, 922–924.
- (2) Campagnola, P. J.; Loew, L. M. Second-harmonic imaging microscopy for visualizing biomolecular arrays in cells, tissues and organisms. *Nat. Biotechnol.* **2003**, *21*, 1356–1360.
- (3) Squier, J.; Muller, M.; Brakenhoff, G.; Wilson, K. R. Third harmonic generation microscopy. *Opt. Express* **1998**, *3*, 315–324.
- (4) Campagnola, P. J.; de Wei, M.; Lewis, A.; Loew, L. M. High-Resolution Nonlinear Optical Imaging of Live Cells by Second Harmonic Generation. *Biophys. J.* **1999**, *77*, 3341–3349.
- (5) Hoover, E. E.; Squier, J. A. Advances in multiphoton microscopy technology. *Nat. Photonics* **2013**, *7*, 93–101.
- (6) Hell, S. W.; Wichmann, J. Breaking the diffraction resolution limit by stimulated emission: stimulated-emission-depletion fluorescence microscopy. *Opt. Lett.* **1994**, *19*, 780–782.
- (7) Rodriguez, A.; Soljacic, M.; Joannopoulos, J. D.; Johnson, S. G.  $\chi^{(2)}$  and  $\chi^{(3)}$  harmonic generation at a critical power in inhomogeneous doubly resonant cavities. *Opt. Express* **2007**, *15*, 7303–7318.
- (8) Baron, A.; Rysanyanskiy, A.; Dubreuil, N.; Delaye, P.; Tran, Q. V.; Combr e, S.; de Rossi, A.; Frey, R.; Roosen, G. Light localization induced enhancement of third order nonlinearities in a GaAs photonic crystal waveguide. *Opt. Express* **2009**, *17*, 552–557.
- (9) Corcoran, B.; Monat, C.; Grillet, C.; Moss, D. J.; Eggleton, B. J.; White, T. P.; O'Faolain, L.; Krauss, T. F. Green light emission in silicon through slow-light enhanced third-harmonic generation in photonic-crystal waveguides. *Nat. Photonics* **2009**, *3*, 206–210.
- (10) Gerard, J. M.; Sermage, B.; Gayral, B.; Legrand, B.; Costard, E.; Thierry-Mieg, V. Enhanced spontaneous emission by quantum boxes in a monolithic optical microcavity. *Phys. Rev. Lett.* **1998**, *81*, 1110–1113.
- (11) Benisty, H.; Weisbuch, C.; Lailly, D.; Rattier, M.; Smith, C. J. M.; Krauss, T. F.; De la Rue, R. M.; Houdre, R.; Oesterle, U.; Jouanin, C.; Cassagne, D. Optical and confinement properties of two-dimensional photonic crystals. *J. Lightwave Technol.* **1999**, *17*, 2063–2077.
- (12) David, S.; El Kurdi, M.; Boucaud, P.; Chelnokov, A.; Le Thanh, V.; Bouchier, D.; Lourtioz, J. M. Two-dimensional photonic crystals with Ge/Si self-assembled islands. *Appl. Phys. Lett.* **2003**, *83*, 2509–2511.
- (13) Le Thomas, N.; Houdr e, R.; Kotlyar, M. V.; O'Brien, D.; Krauss, T. F. Exploring light propagating in photonic crystals with Fourier optics. *J. Opt. Soc. Am. B* **2007**, *24*, 2964–2971.
- (14) Bonato, C.; Hagemeyer, J.; Gerace, D.; Thon, S. M.; Kim, H.; Andreani, L. C.; Petroff, P. M.; van Exter, M. P.; Bouwmeester, D. Far-field emission profiles from L3 photonic crystal cavity modes. *Phot. and Nanostruc. - Fundamentals and Applications* **2013**, *11*, 37–47.
- (15) Moreaux, L.; Sandre, O.; Charpak, S.; Blanchard-Desce, M.; Mertz, J. Coherent Scattering in Multi-Harmonic Light Microscopy. *Biophys. J.* **2001**, *80*, 1568–1574.
- (16) McCutcheon, M. W.; Young, J. F.; Rieger, G. W.; Dalacu, D.; Fr ed eric, S.; Poole, P. J.; Williams, R. L. Experimental demonstration of second-order processes in photonic crystal microcavities at submilliwatt excitation powers. *Phys. Rev. B: Condens. Matter Mater. Phys.* **2007**, *76*, 245104.
- (17) Rivoire, K.; Lin, Z.; Hatami, F.; Masselink, W. T.; Vučkovi c, J. Second harmonic generation in gallium phosphide photonic crystal nanocavities with ultralow continuous wave pump power. *Opt. Express* **2009**, *17*, 22609–22615.
- (18) Galli, M.; Gerace, D.; Welna, K.; Krauss, T. F.; O'Faolain, L.; Guizzetti, G.; Andreani, L. C. Low-power continuous-wave generation of visible harmonics in silicon photonic crystal nanocavities. *Opt. Express* **2010**, *18*, 26613–26624.
- (19) Buckley, S.; Radulaski, M.; Petykiewicz, J.; Lagoudakis, K. G.; Kang, J.-H.; Brongersma, M.; Biermann, K.; Vučkovi c, J. Second-Harmonic Generation in GaAs Photonic Crystal Cavities in (111)B and (001) Crystal Orientations. *ACS Photonics* **2014**, *1*, 516–523.
- (20) Yamada, S.; Song, B.-S.; Jeon, S.; Upham, J.; Tanaka, Y.; Asano, T.; Noda, S. Second-harmonic generation in a silicon-carbide-based photonic crystal nanocavity. *Opt. Lett.* **2014**, *39*, 1768–1771.
- (21) Zeng, Y.; Roland, I.; Checoury, X.; Han, Z.; El Kurdi, M.; Sauvage, S.; Gayral, B.; Brimont, C.; Guillet, T.; Mexis, M.; Semond, F.; Boucaud, P. Resonant second harmonic generation in a gallium nitride two-dimensional photonic crystal on silicon. *Appl. Phys. Lett.* **2015**, *106*, 081105.
- (22) Torres, J.; Coquillat, D.; Legros, R.; Lascaray, J. P.; Teppe, F.; Scalbert, D.; Peyrade, D.; Chen, Y.; Briot, O.; Le Vassor d'Yerville, M.; Centeno, E.; Cassagne, D.; Albert, J. P. Giant second-harmonic generation in a one-dimensional GaN photonic crystal. *Phys. Rev. B: Condens. Matter Mater. Phys.* **2004**, *69*, 085105.
- (23) Coquillat, D.; Vecchi, G.; Comaschi, C.; Malvezzi, A. M.; Torres, J.; Le Vassor d'Yerville, M. Enhanced second- and third-harmonic generation and induced photoluminescence in a two-dimensional GaN photonic crystal. *Appl. Phys. Lett.* **2005**, *87*, 101106.
- (24) Xiong, C.; Pernice, W. H. P.; Sun, X.; Schuck, C.; Fong, K. Y.; Tang, H. X. Aluminum nitride as a new material for chip-scale optomechanics and nonlinear optics. *New J. Phys.* **2012**, *14*, 095014.
- (25) Xiong, C.; Pernice, W.; Ryu, K. K.; Schuck, C.; Fong, K. Y.; Palacios, T.; Tang, H. X. Integrated GaN photonic circuits on silicon (100) for second harmonic generation. *Opt. Express* **2011**, *19*, 10462–10470.
- (26) Chicanne, C.; David, T.; Quidant, R.; Weeber, J. C.; Lacroute, Y.; Bourillot, E.; Dereux, A.; Colas des Francs, G.; Girard, C. Imaging the Local Density of States of Optical Corrals. *Phys. Rev. Lett.* **2002**, *88*, 097402.
- (27) Rotenberg, N.; Kuipers, L. Mapping nanoscale light fields. *Nat. Photonics* **2014**, *8*, 919–926.
- (28) La China, F.; Intonti, F.; Caselli, N.; Lotti, F.; Vinattieri, A.; Vico Trivi no, N.; Carlin, J.-F.; Butt e, R.; Grandjean, N.; Gurioli, M. Vectorial near-field imaging of a GaN based photonic crystal cavity. *Appl. Phys. Lett.* **2015**, *107*, 101110.
- (29) Dharanipathy, U.; Vico Trivi no, N.; Yan, C.; Diao, Z.; Carlin, J.-F.; Grandjean, N.; Houdr e, R. Near-infrared characterization of gallium nitride photonic-crystal waveguides and cavities. *Opt. Lett.* **2012**, *37*, 4588–4590.
- (30) Vico Trivi no, N.; Dharanipathy, U.; Carlin, J.-F.; Diao, Z.; Houdre, R.; Grandjean, N. Integrated photonics on silicon with wide bandgap GaN semiconductor. *Appl. Phys. Lett.* **2013**, *102*, 081120.
- (31) Roland, I.; Zeng, Y.; Han, Z.; Checoury, X.; Blin, C.; El Kurdi, M.; Ghrib, A.; Sauvage, S.; Gayral, B.; Brimont, C.; Guillet, T.; Semond, F.; Boucaud, P. Near-infrared gallium nitride two-dimensional photonic crystal platform on silicon. *Appl. Phys. Lett.* **2014**, *105*, 011104.
- (32) Sam-Giao, D.; N eel, D.; Sergent, S.; Gayral, B.; Rashid, M. J.; Semond, F.; Duboz, J. Y.; Mexis, M.; Guillet, T.; Brimont, C.; David, S.; Checoury, X.; Boucaud, P. High quality factor AlN nanocavities

embedded in a photonic crystal waveguide. *Appl. Phys. Lett.* **2012**, *100*, 191104.

(33) Kuramochi, E.; Notomi, M.; Mitsugi, S.; Shinya, A.; Tanabe, T.; Watanabe, T. Ultrahigh-Q photonic crystal nanocavities realized by the local width modulation of a line defect. *Appl. Phys. Lett.* **2006**, *88*, 041112.

(34) Han, Z.; Chécoury, X.; Néel, D.; David, S.; El Kurdi, M.; Boucaud, P. Optimized design for 2 million ultra-high Q silicon photonic crystal cavities. *Opt. Commun.* **2010**, *283*, 4387–4391.

(35) Miragliotta, J.; Wickenden, D. K. Optical third-harmonic studies of the dispersion in  $\chi^{(3)}$  for gallium nitride thin films on sapphire. *Phys. Rev. B: Condens. Matter Mater. Phys.* **1994**, *50*, 14960–14964.

(36) Joannopoulos, J. D., Winn, J. N., Johnson, S. G., Meade, R. D. *Photonic Crystals: Molding the Flow of Light*, 2nd ed.; Princeton University Press, 2008.

(37) Rivoire, K.; Buckley, S.; Vučković, J. Multiply resonant photonic crystal nanocavities for nonlinear frequency conversion. *Opt. Express* **2011**, *19*, 22198–22207.

(38) Boyd, R. W. In *Nonlinear Optics*, 3rd ed.; Academic Press: Burlington, 2008; pp 1–67.

(39) Streibl, N. Three-dimensional imaging by a microscope. *J. Opt. Soc. Am. A* **1985**, *2*, 121–127.

(40) Kim, M.-S.; Scharf, T.; Menzel, C.; Rockstuhl, C.; Herzig, H. P. Talbot images of wavelength-scale amplitude gratings. *Opt. Express* **2012**, *20*, 4903–4920.

(41) Zhang, Y.; Wen, J.; Zhu, S. N.; Xiao, M. Nonlinear Talbot Effect. *Phys. Rev. Lett.* **2010**, *104*, 183901.